Exoplanet coronagraph shaped pupil masks and laboratory scale star shade masks: Design, Fabrication and Characterization

Kunjithapatham Balasubramanian[a], Victor White[a], Karl Yee[a], Pierre Echternach[a], Richard Muller[a], Matthew Dickie[a], Eric Cady[a], Camilo Mejia Prada[a], Daniel Ryan[a], Ilya Poberezhskiy[a], Hanying Zhou[a], Brian Kern[a], A.J. Riggs[b], Neil T. Zimmerman[b], Dan Sirbu[b], Stuart Shaklan[a], and Jeremy Kasdin[b]
[a]Jet Propulsion Laboratory, California Institute of Technology,
4800 Oak Grove Drive, Pasadena, CA 91109
[b]Mechanical & Aerospace Engineering, Princeton University, Princeton, NJ 08544

ABSTRACT

Star light suppression technologies to find and characterize faint exoplanets include internal coronagraph instruments as well as external star shade occulters. Currently, the NASA WFIRST-AFTA mission study includes an internal coronagraph instrument to find and characterize exoplanets. Various types of masks could be employed to suppress the host star light to about 10^{-9} level contrast over a broad spectrum to enable the coronagraph mission objectives. Such masks for high contrast internal coronagraphic imaging require various fabrication technologies to meet a wide range of specifications, including precise shapes, micron scale island features, ultra-low reflectivity regions, uniformity, wave front quality, achromaticity, etc. We present the approaches employed at JPL to produce pupil plane and image plane coronagraph masks by combining electron beam, deep reactive ion etching, and black silicon technologies with illustrative examples of each, highlighting milestone accomplishments from the High Contrast Imaging Testbed (HCIT) at JPL and from the High Contrast Imaging Lab (HCIL) at Princeton University. We also present briefly the technologies applied to fabricate laboratory scale star shade masks.

Keywords: WFIRST-AFTA, Exoplanet, Coronagraph, Shaped Pupil Masks, star shade, external occulter.

1. INTRODUCTION

Imaging faint exoplanets orbiting around bright stars requires advanced coronagraph techniques to suppress the host starlight in the image plane of a telescope to a level of about 10^{-9} or better. The NASA WFIRST-AFTA mission includes a coronagraph instrument to enable such an objective. Various coronagraph architectures are being developed for this purpose to advance the technology to Technology Readiness Level 5 (TRL 5) in 2016. Central to all coronagraphs are starlight suppressing masks to function either in the focal plane or pupil plane or both. Hybrid Lyot Coronagraph[1-4] (HLC), Shaped Pupil Coronagraph[5,6] (SPC), and Phase Induced Amplitude Apodization Complex Mask Coronagraph[7-11] (PIAACMC) are among such architectures suitable for obscured telescope pupils. In December 2013, based on a study conducted by the AFTA Coronagraph Working Group (ACWG), NASA announced the selection of the Occulting Mask Coronagraph (OMC) as the primary architecture for the WFIRST coronagraph instrument. OMC will operate between Hybrid Lyot and Shaped Pupil modes to find and characterize exoplanets by exploiting the strengths of each. Both architectures are currently being matured through technology development with a set of nine milestones approved by NASA to be passed during 2014-2016 to reach TRL 5 by September 2016. The first four of these milestones have been passed successfully as of March 2015. In this paper, we discuss the details which relate to the first milestone of SPC, i.e., the fabrication, characterization and performance of SPC masks; details of the second SPC milestone, a testbed demonstration are discussed in a companion paper[12] (Cady, *et al 2015*).

kbala@jpl.nasa.gov; phone: 818-393-0258

1.1 Background on Shaped Pupil Coronagraph Masks

Modifying the amplitude of the star light optical field as presented by the telescope assembly at the pupil of the coronagraph instrument is one of the viable techniques to adequately suppress star light in the image plane. A simple circular pupil of an unobscured telescope produces a typical Airy pattern at the image with a Fourier transform relationship. An appropriately modified pupil can produce dark regions in the image by diffraction that can be computed and optimized. This simple concept behind the "shaped pupil coronagraph" (SPC) as illustrated in Fig. 1 has been demonstrated by laboratory experiments[5] at Princeton University and at JPL[13,14]. Different kinds of masks, i.e., pupil plane masks and associated focal plane masks with unique shapes, sizes and features, need different technologies to produce them[13,14,15]. Masks for such shaped pupils have been designed by the Princeton University team and fabricated as free standing transmitting devices by the JPL team[15,16]. These masks, an example of which is shown in Fig. 1, incorporate transparent and opaque shapes with slits and micron scale features. Such devices have been fabricated successfully on silicon wafers employing electron beam lithography and deep reactive ion etching techniques to the required feature accuracies. Industry standard silicon-on-insulator (SOI) wafers consisting of a thin "device layer" (typically 10 to 50 microns thick) on a thick "handle wafer" (typically 300 to 500 microns thick) of silicon separated by a very thin silicon oxide insulator layer (typically 1 micron thick) are employed for fabricating these devices. The typical cross section of the shaped slits shown in Fig. 2 illustrates the use of such an SOI wafer with the thinner layer defining the slit edge. The narrow slit ends were dithered with pin holes as seen in Fig. 2(c) and 2(e) to approximate the effect of thinner slits that could not be fabricated accurately enough. The scanning electron microscope (SEM) images in Fig. 2(b) and 2 (c) and the high resolution optical image in Fig. 2 (e) show the details of the slit shapes and cross section. Such freestanding and self-supporting masks have been tested at Princeton University High Contrast Imaging Lab (HCIL) (Belikov *et al.*, 2006, 2007)[5,13].

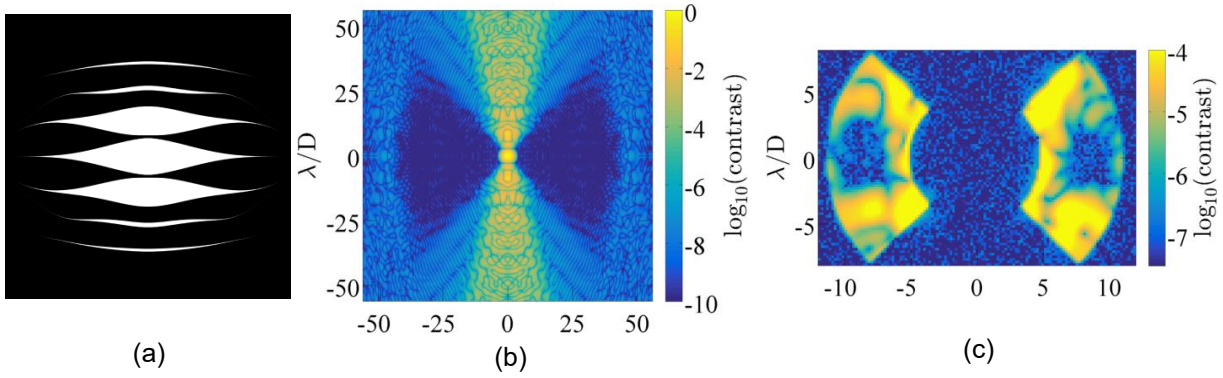

Figure 1: (a) Ripple3 SPC design (a) used in the HCIT in 2007 by Belikov et al. and currently used in Princeton's HCIL. (b) The PSF per design with 3e-10 contrast from 4-40 λ/D over symmetric 90-degree sectors. The ideal PSF simply scales with wavelength. (c) Princeton HCIL best monochromatic contrast result of 1.2e-7 after 2-DM wavefront correction in symmetric dark holes from 7-10 λ/D in x and -3 to 3 λ/D in y. (Riggs, *et al*, 2015)[17].

In the Princeton HCIL testbed, a similar SPC mask named Ripple 3, shown in Fig. 1 (a), was used with two Boston Micromachines kilo-DM deformable mirrors in series in the testbed operating in air. Small symmetric dark holes from +/-(7-10) λ/D in x and -3 to 3 λ/D in y were used because the HCIL DMs did not have enough stroke to correct a larger area and/or smaller inner working angle (IWA). The HCIL's monochromatic contrast floor after wavefront correction was 1.2e-7 (as shown in Fig. 1 c)[17] because of detector noise and large optical errors unknown to the controller model. Large aberrations and limited DM actuator stroke limited the HCIL broadband performance to 6e-6 in 10% light [Groff, [18], 2011, Groff [19] 2013].

The free standing transmissive shaped pupil mask image shown in Fig. 2 (d) was designed and fabricated in 2013 for the JPL High Contrast Imaging Testbed (HCIT) with unobscured pupil.

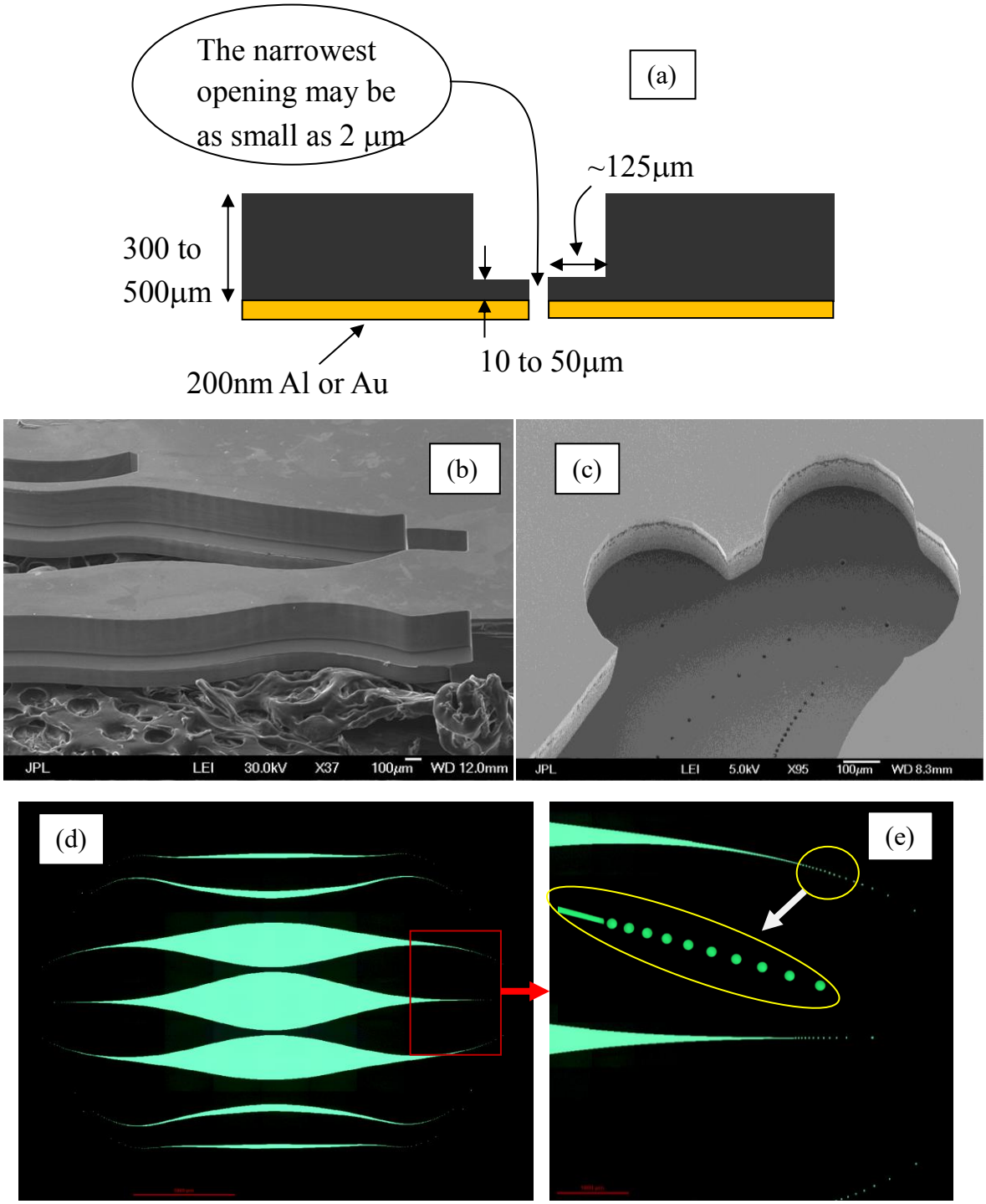

Figure 2. (a) Cross section of DRIE etched slits; the recessed walls and thinned edges help in controlling scattered light from the rough walls and to reduce wave guiding effects (b) An example SEM image of the cross section of a typical slit edge in the transmissive shaped pupil mask, (c) Another example SEM image viewed from the thick back side showing a series of pin holes at the end of slit in the thin side of SOI wafer, (d) Transmission image of a free-standing shaped pupil mask designed by Princeton University team and fabricated at JPL for 30mm dia HCIT unobscured pupil, (e) Image of the dashed edges of the ends of the mask slits with 25 micron size scale pin holes.

The HCIT successfully demonstrated[20] in June 2013 (Riggs *et al,* 2013) a high contrast of $4x10^{-9}$ in monochromatic, 790 nm laser light with 2DMs. Figure 3(a) shows the design of a manufactured mask that was tested in the HCIT. Fig 3 (c) shows the achieved contrast in 5 to 11 λ/D dark hole in the final image.

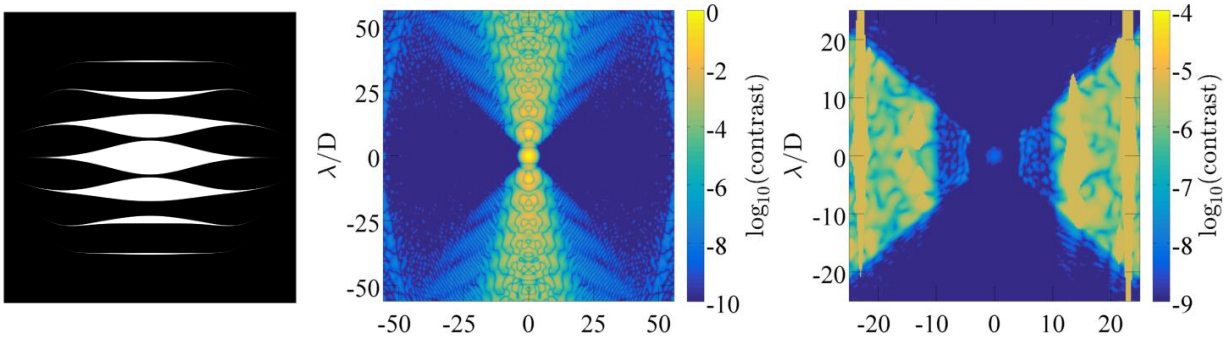

Figure 3 (a) Ideal design of the SPC mask. (b) Ideal PSF of this SPC on a log10 scale, with 1e-10 average contrast in a region from 4.5-56 λ/D in symmetric 90-degree sectors. (c) Monochromatic PSF at 790nm after wavefront correction with 2 DMs in series in the HCIT for the first time. The achieved contrast was 3.6e-9 from 5 λ/D (in radius) to 11 λ/D (in x) over 85-degree sectors by Riggs *et al.*[20].

2. SPC MASKS FOR WFIRST-AFTA CORONAGRAPH

The WFIRST-AFTA telescope with obscured pupil geometry due to a slightly off-axis secondary and support structures presents challenges for implementing transmissive masks because the 2-D optimized designs to reach high contrast almost always contain island structures on the mask[21, 22] (Carlotti *et al*., 2011 and Vanderbei 2012) that cannot be free-standing and self-supporting with sufficient structural integrity. Transparent substrates are problematic because of dispersion induced chromatic wavefront errors as well as surface reflections leading to ghost images. New, but yet to be mature, options for transmissive masks with island structures are discussed in section 8 on future directions. To surmount these challenges, new approaches were considered to fabricate the shaped pupil masks with island features. Reflecting devices with extremely black structures in a highly reflective background have been developed for this purpose as discussed in the following sections. Cryogenic reactive ion etching techniques were developed to create such black islands on an aluminum coated silicon substrate, thus providing very high reflectivity contrast between adjacent regions on the mask. This unique reflective shaped pupil (RSP) mask concept is illustrated in Fig.4.

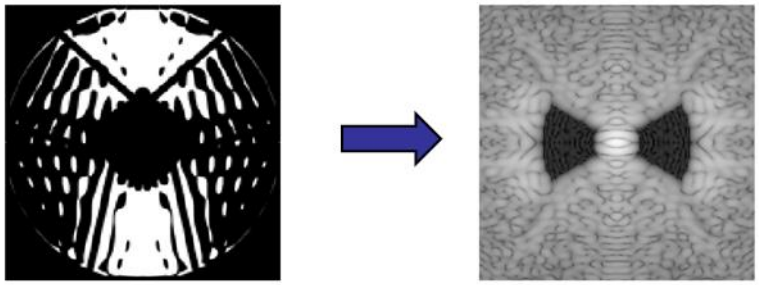

Figure 4. Reflective shaped pupil coronagraph concept: highly absorbing shapes on a highly reflective surface to modify the pupil plane field in the coronagraph to produce the dark hole regions in the image plane shown on the right.

3. THE TECHNOLOGY TO FABRICATE BLACK SILICON DEVICES

A polished silicon surface has a typical reflectivity of about 35% in the visible spectrum. But, micro and nano scale structures on the surface can reduce the reflectivity significantly through absorption and scattering. The micro structure modifies the effective refractive index of the material surface and achieves extremely low broadband reflectance due to high absorption and diffuse scattering at the structured silicon surface. A cryogenic reactive ion etching (CRIE) with

inductively coupled plasma (ICP) process has been developed at JPL to create sub-micron needle structures that extend deep into the silicon surface. Figure 5 shows the nanostructure of the black silicon surface produced by CRIE with the Oxford ICP RIE system at Caltech KNI (Kavli Nanoscience Institute). The "blackness" achievable depends on the nature of the silicon wafer and the process details. We employed a highly doped p type Si wafer with <100> orientation, though other orientations may also perform as well. Process optimization has yielded black silicon surfaces with extremely low reflectivity over a broad band as detailed below. CRIE[23,24] is an alternative to the standard Bosch process[25,26] for achieving anisotropic etch profiles in silicon. In both processes, SF6 is used as the Si etch gas. In the CRIE process O2 gas flowed into the chamber combines with the silicon/SF6 etch by-products, and at cryogenic temperatures the SiOxFy condensate continuously forms a sidewall passivation layer, preventing later etching; the passivation at the bottom of the trenches is easily sputtered away by directional ion bombardment, enabling the creation of trenches with near vertical sidewalls. Flow through of excess O2 gas results in over passivation at the bottom of trenches; precise control of the O2 flow to maintain the condition of the onset of the over-passivation condition will result in micro-masking, enabling etching of random nanopillar arrays without the need for a lithographically defined etch mask. The passivation layer sublimates upon warming of the wafer, and thus does not require chemical removal. The process sequence is illustrated in Table 1 below.

2mm to 5mm thick base Silicon wafer	
Apply ~200nm of Al layer	
Spin on photoresist on aluminum, then expose and develop pattern on photoresist	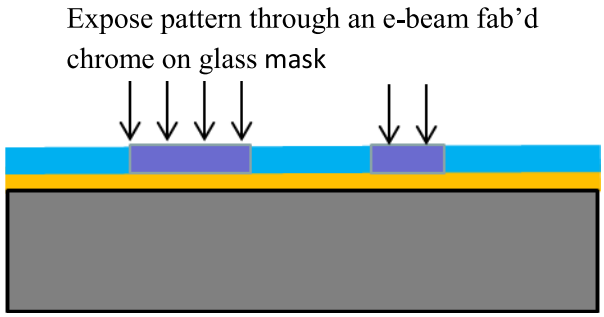
Use chlorine (ICP-RIE) plasma to etch exposed aluminum all the way to the silicon; Resist on aluminum provides a perfect "self alignment" and protects it during subsequent cryoetch of silicon	
ICP cryo etch to create black Si pattern on wafer. Remove passivating resist layer after ICP cryo etch and dicing of chips	

Table 1. Black silicon mask pattern fabrication process

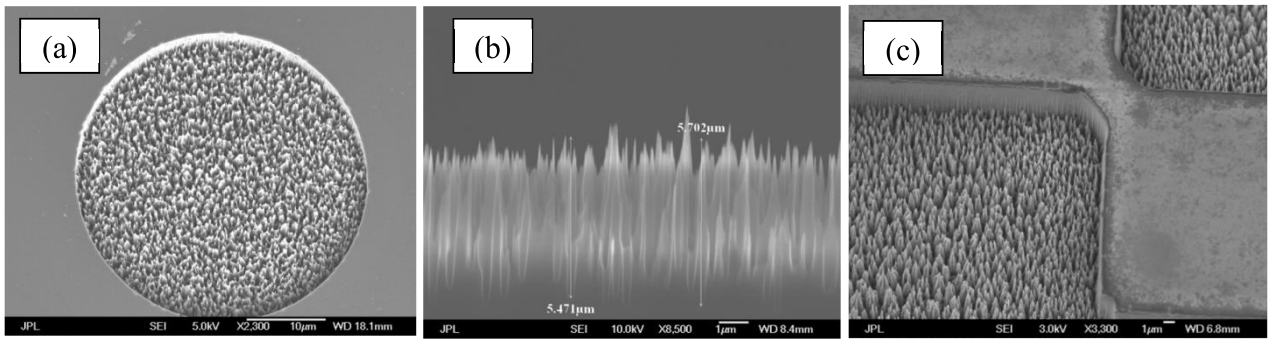

Figure. 5 (a). SEM image of typical black Si surface (b). SEM cross section image of typical black Si surface (c) SEM image of a mask feature with black silicon adjacent to metal features

3.1 Measurement of "blackness" and achieved low reflectance

The total integrated hemispherical reflectance (diffuse + specular) of the black silicon surface has been measured over the required 400 to 1000 nm spectral band. The nearly Lambertian diffuse reflection occurs due to the "roughness" of the surface (Fig.5), where the light undergoes large excursions and absorption. A Perkin Elmer 1050 spectrophotometer attached with an integrating sphere with a 1 inch sample port was employed to measure the integrated total reflectance (specular + scattered) of several black silicon samples over the visible spectrum. Figure 6 shows the measured results with less than 0.3% total reflectance in the 500 to 800 nm band. The samples, both the device under test and a calibrated Spectralon reference sample from Labsphere Inc., were measured at 8° angle of incidence. For an interesting comparison, black samples of anodized aluminum, a black painted metal, a commercial Acktar black material and our black Si were measured, demonstrating the extreme blackness achievable with black Si as seen in Fig. 7.

The spectrophotometer, however, does not have the sensitivity to measure the very low specular reflectance of black silicon. In order to measure this critical parameter, we assembled a dedicated laboratory setup with a stabilized HeNe laser and a ½" CMOS digital camera as shown in Fig. 8. The DataRay WinCamD UHR CMOS camera has a 1280x1024 array with 5.3x6.6 mm sensor area with 5.2 µm pixels and 10 bit ADC with 43dB dynamic range.

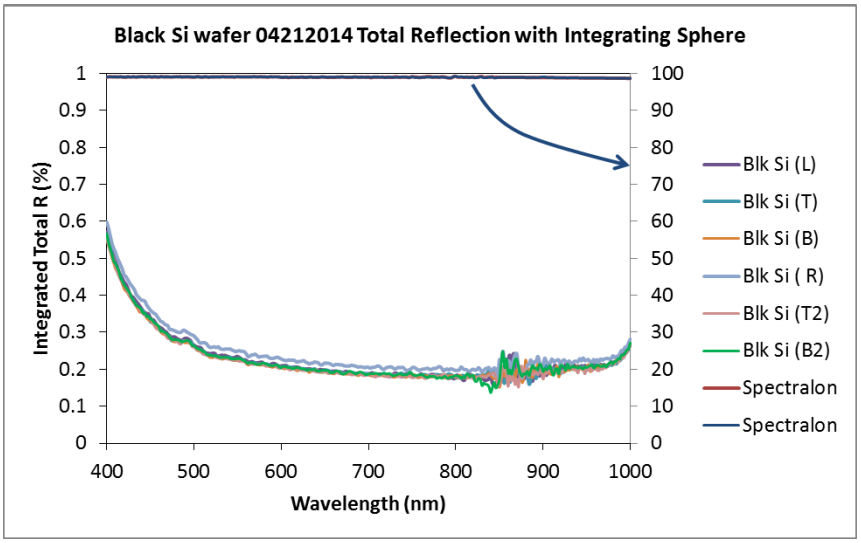

Figure 6. Total hemispherical reflectance (specular + diffuse at 8 deg AOI) of a black silicon sample (left axis) measured with an integrating sphere on a PE 1050 spectrophotometer, calibrated with LabSphere Spectralon reference standard. Noise beyond 850 nm is due to a detector change in the system. Chart shows multiple measurements across several locations (left, right, top and bottom areas) on a large blackened Si wafer

The setup uses a stabilized 633 nm HeNe laser whose collimated beam passes through a wheel with several neutral density (ND) filters and is reflected off a shaped pupil mask under test. The mask has both highly reflective aluminum coated regions and black silicon regions and can be translated transversely so that the laser beam hits either of the two regions, as shown in Fig. 8 (b). The detector (either a discrete photodiode or a digital camera) is centered on the specular reflection of the beam when the laser light is reflected from the aluminum coated region. The optical powers reflected from the aluminum and black silicon regions on the same sample are measured and compared. Several

measurements were made with the detector moved transversely to and along the beam to separate diffuse and specular components. The setup was fully enclosed in a black box to minimize the ambient light leakage into the measurement.

Employing calibrated ND filters from OD 1 to OD 6 in the optical path enables extending the measurement dynamic range and allows performing a calibration of the measurement accuracy. Newport 818-SL detector and 1830-C low-noise power meter were used in the measurement. While the total (diffuse + specular) reflectance is about 0.2% at 633nm as seen in figures 6 and 7 per measurements on the spectrophotometer, the most conservative measured value of the specular reflectance with this monochromatic set up was R_s=7×10^{-8} at 633nm wavelength as shown in Fig. 9. This value was limited by the measurement setup sensitivity and the actual value is likely to be significantly lower. In fact, the reflection off black silicon shows no prominent specular component, as seen in Fig. 9 taken with the WinCamD CMOS camera described above. The typical laser spot size was ~ 1.5mm and the laser power was ~1.5mW. Multiple measurements were made to estimate the average reflectance ratios from several spots.

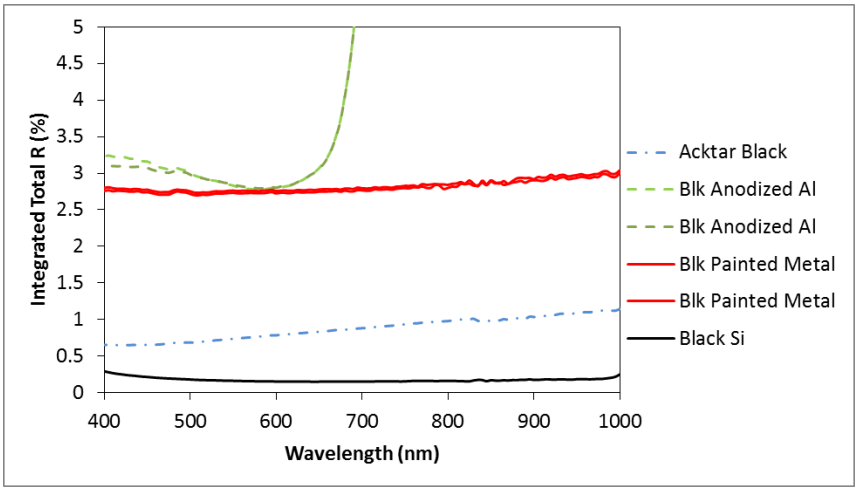

Figure 7. Comparison of measured total integrated reflectance (specular + diffuse) of samples of commercial Acktar black material, black anodized aluminum, a black painted metal, and black Si wafer illustrating the extreme blackness achievable with another black Si sample

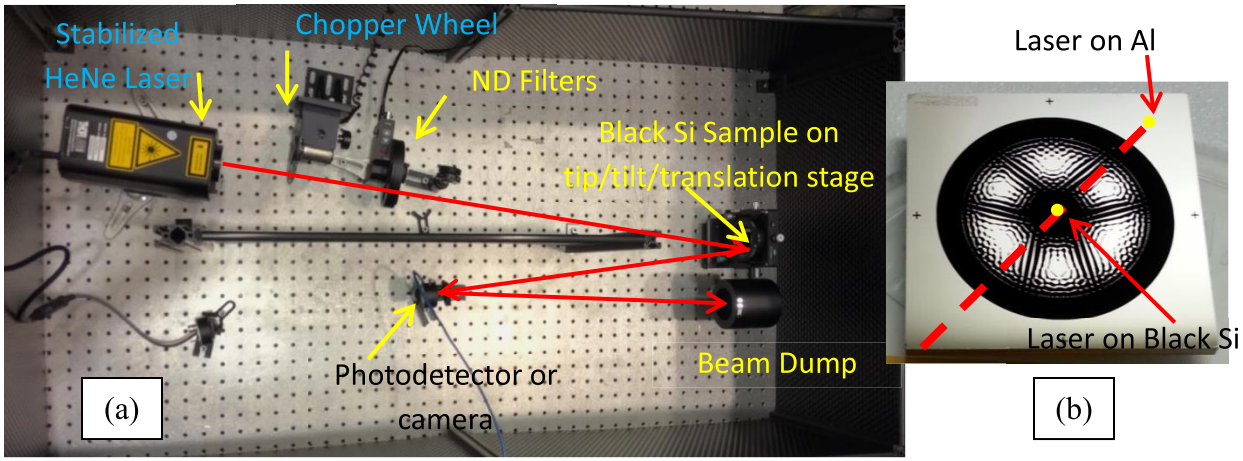

Figure 8. (a) A dedicated lab setup for measuring black silicon reflectance. Neutral density filters (OD 1 to OD 6) extend the dynamic range and allow measurement calibration. (b) Translating the sample between aluminum-coated and black silicon regions calibrates out common-mode testbed losses.

3.2 First reflective shaped pupil mask with black silicon structures designed and fabricated for unobscured pupil

Initially, we designed a reflective shaped pupil mask for unobscured pupil geometry for the Princeton HCIL testbed. This mask contained islands of black regions in a reflective background, thus forming a nearly binary reflective SPC

mask. The minimum feature size was 20 µm x 20 µm square on a 10 mm diameter pupil area. A commercial grade silicon wafer of ~500 µm thickness was lithographically patterned with a protective photoresist exposing only the areas to be blackened. Then the cryogenic reactive ion etching process was employed to etch deep nano structures on the exposed regions of the wafer. Finally the protective resist was cleaned off leaving a binary pattern of mask with "black and white" structures. The fabrication process methodology to produce such masks is illustrated in Table 1. Figure 10 (a) shows an image of the first reflective shaped pupil mask fabricated in Feb 2013 proving the feasibility to employ black silicon technology to produce such masks. A zoomed-in view of the fine features of the mask is seen in Fig. 10 (b). Ideal design performance with such a mask and experimentally observed image in Princeton HCIL are shown in Fig. 11.

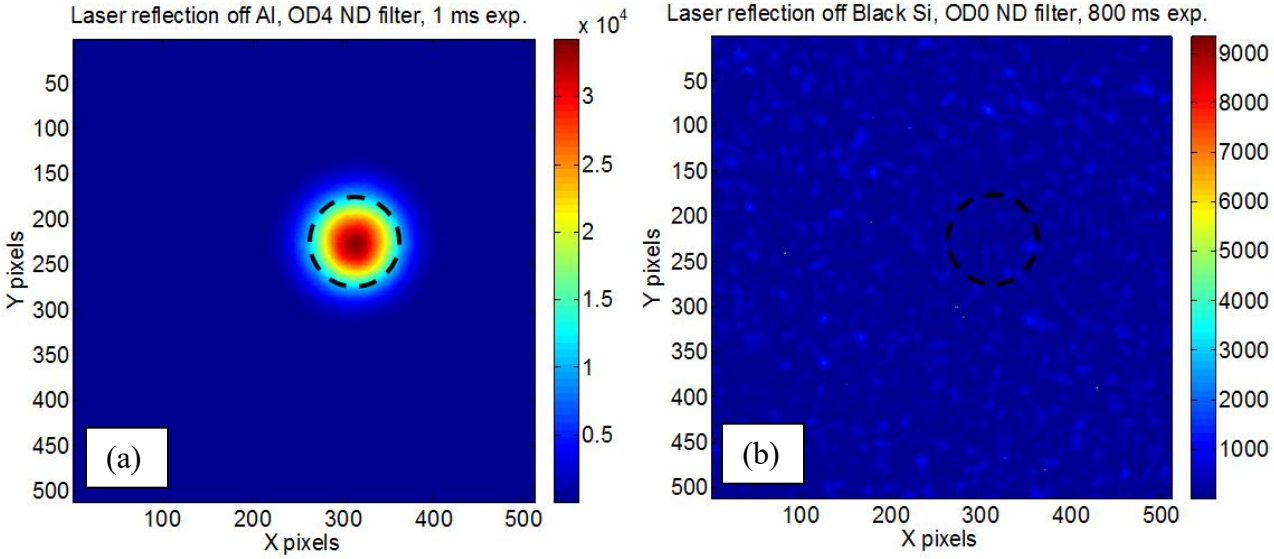

Figure 9. Comparison of camera images with laser beam reflecting off (a) aluminum coated region and (b) black silicon region. Speckle morphology of black Si reflection shows no detectable specular reflection peak. Dotted circles show $1/e^2$ intensity location on the laser spot.

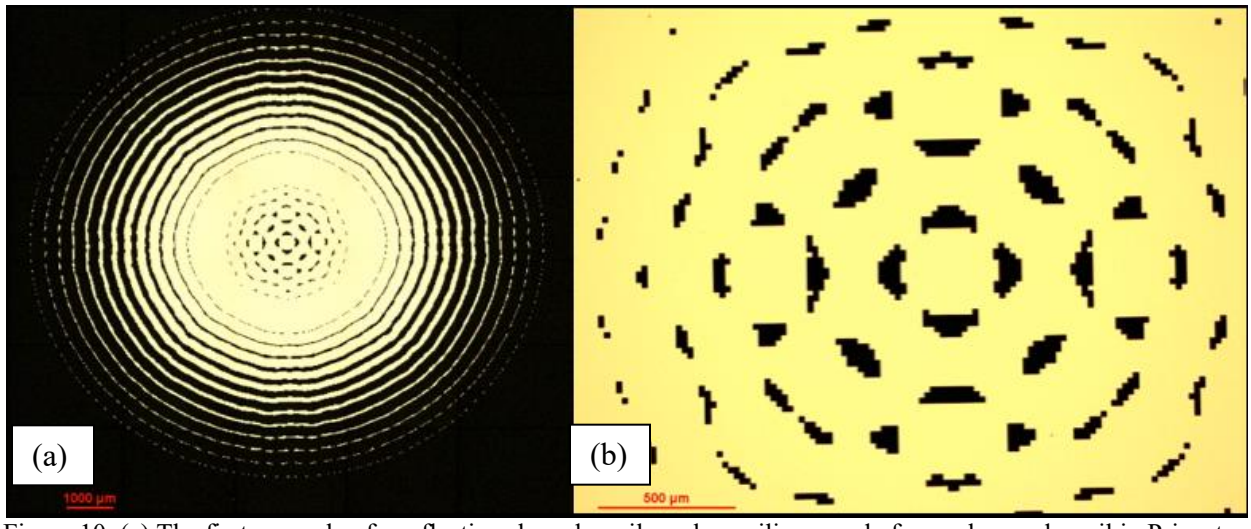

Figure 10. (a) The first example of a reflective shaped pupil mask on silicon made for unobscured pupil in Princeton HCIL testbed. (b) The image on the right is an enlarged view of the central region of the mask with 20µm x 20µm minimum feature size. The mask design is stretched 23.7 degrees along the horizontal axis before manufacture to project a circular mask on the incident beam.

Subsequently in Nov 2013, aluminum coated Si wafers were employed to fabricate such reflective shaped pupil masks successfully with the same design and process.

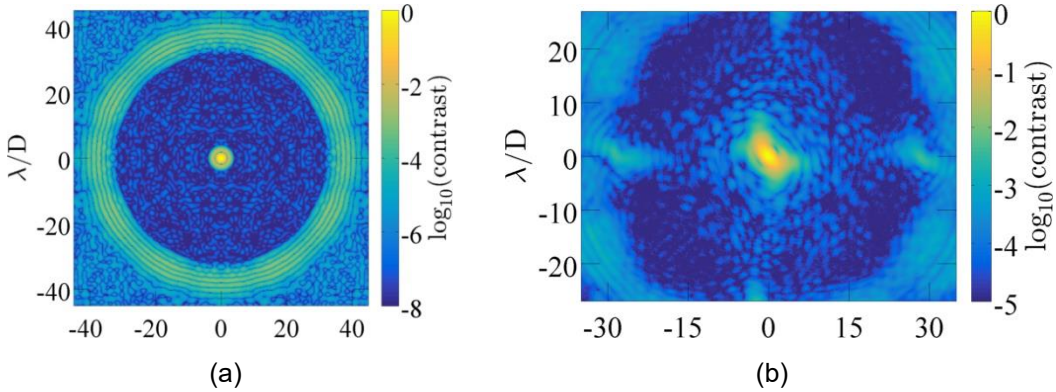

Figure. 11. (a) The ideal simulated PSF plot on a log10 scale of the ideal shape of the mask shown in Fig 10. The ideal PSF gives a contrast is 8e-8 from 4-32 λ/D in a 360-degree region. (b) Image of the PSF without wavefront correction in Princeton's HCIL experiment (right). The large low-order aberrations from the 0.5mm-thick mask substrate causes the elongation of the PSF in the laboratory image. The spots in (b) at +/- 30 λ/D are copies of the PSF from the nominal quilting pattern on the DMs. The PSF in (b) was measured at Princeton's HCIL without wavefront correction. The contrast around the PSF core is several orders of magnitude worse than the ideal PSF because of the nominal HCIL optical aberrations.

4. DESIGNS FOR OBSCURED TELESCOPE PUPIL

Princeton HCIL members have developed software tools to numerically optimize binary shaped pupil masks for arbitrary two-dimensional telescope apertures[21,22] (Carlotti, *et al*., 2011, Vanderbei *et al.*, 2012). For the case of an AFTA-like telescope pupil, with a large central obstruction and six support struts, two categories of solutions were explored (Carlotti, *et al*.[6], 2013):

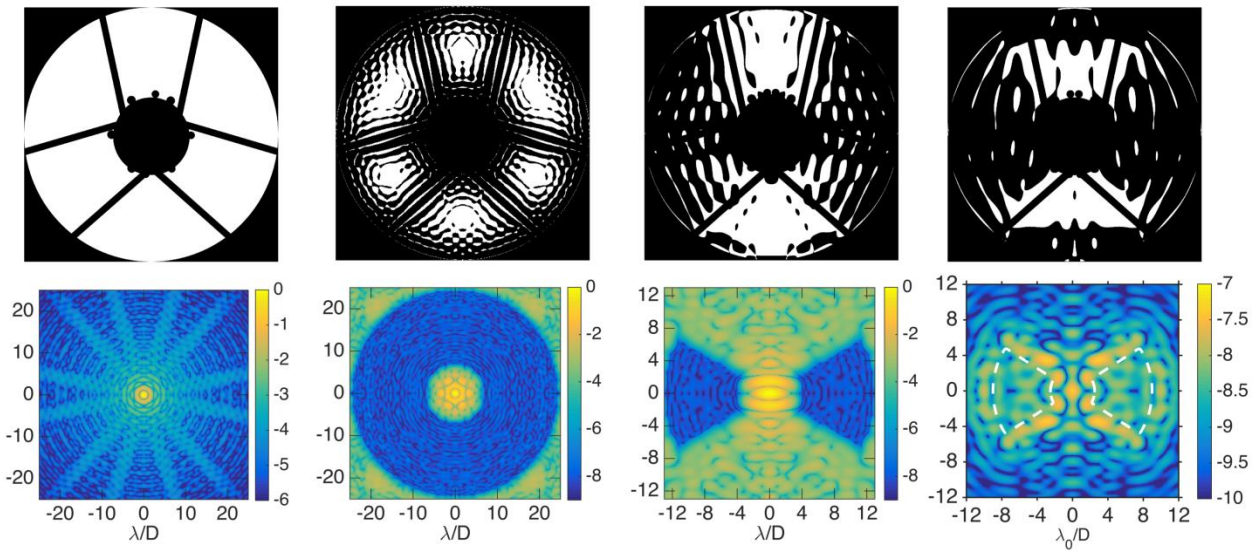

Figure 12. Shaped pupils, each with its corresponding ideal PSF plotted below it on a logarithmic intensity scale. From left to right: AFTA-like telescope pupil, disc science mask, characterization mask (Gen1 SPC), and characterization mask for Lyot configuration (Gen2 SPLC).

i) ***Characterization*** masks that restrict the coronagraph field of view to a bowtie-shaped region in order to achieve a small inner working angle. In the observing scenario when the position of an exoplanet is known, this mode offers an efficient means of acquiring broadband spectra.

ii) ***Discovery*** and ***Disk Science*** masks that create a wider, annular field of view around the star, but with an inner edge further from the star than the *characterization* mode.

These two mask types and further developments (Riggs *et al*[27], Zimmerman *et al*[28]) are illustrated in Fig. 12 with the mask type on the top row and the resulting PSF in the bottom row.

5. WFIRST-AFTA CORONAGRAPH MASK REQUIREMENTS

The mask requirements were set by a of technology demonstration plan (Poberezhskiy *et al* [29]). In particular, the WFIRST-AFTA technology development Milestone 1 was initially defined as: "*First-generation reflective Shaped Pupil apodizing mask fabricated with black silicon specular reflectance of less than 10^{-4} and 20 μm pixel size*", followed by Milestone 2 defined as:

"*The shaped pupil coronagraph in the High Contrast Imaging Testbed demonstrates 10^{-8} raw contrast with narrowband light at 550 nm in a static environment".*

Subsequently, the Milestone 1 criteria was modified to meet a minimum feature size of 22 μm as required on the testbed, and to reach a specular reflectance of less than 10^{-7} from black silicon relative to aluminum coating in order to keep the black Si contribution to less than $3\text{x}10^{-10}$ at 4λ/D in the final image in order to meet the mission science goals. The first two milestones were accomplished successfully with masks fabricated in April 2014, meeting Milestone 1 criteria and testbed results reaching Milestone 2 in Aug/Sep 2014. Further improvements in feature accuracy as well as reflectance and wavefront quality have since been made, in readiness for the Milestone 5 (Sep 2015) requirements "*to demonstrate 10^{-8} raw contrast with 10% broadband light centered at 550 nm in a static environment"*. Details of testbed demonstrations with the help of the Deformable Mirrors (DM) correcting and controlling the wavefront and creating the dark hole through electric field conjugation (EFC) technique can be found in a companion paper of Cady *et al*[12].

5.1 Specular and Diffuse Reflection of Black Silicon

In the context of the SPC, the treatments of the specular and diffuse reflectance of the black Si follow very different analyses. The treatment of the specular reflectance follows a similar analysis to that of the coronagraph itself, with a different "input" illumination. The left-hand panel of Fig. 13 shows the input illumination of the SPC, from the Al reflection (the desired SPC response) and from the specular reflectance of the black Si. The black Si specular reflectance can be quantified by a value R_s, with $0 <= R_s <= 1$.

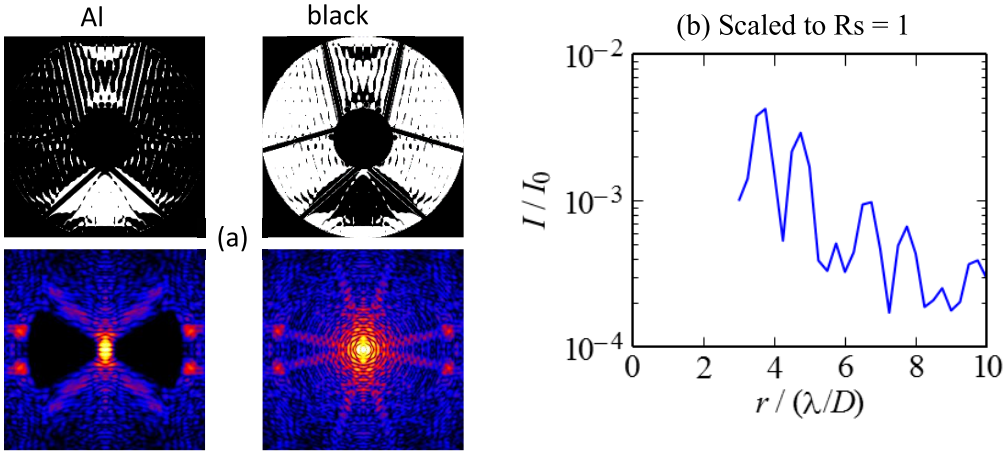

Figure. 13. (a) Pupil-plane distributions of specular reflection from Al and black Si surfaces, and the resulting PSFs, and (b) the image-plane intensity in the dark hole region as a function of radius for the black Si specular reflectance, normalized by the peak Al PSF brightness (I_0), for R_s=1.

The etching process that creates the black Si depresses the height of the black Si surface by a distance on the order of 10 μm, relative to the location of the Al surface. At this distance, for all but very narrow bandpasses ($\Delta\lambda/\lambda < 5\%$), the wavefront reflected from the Al and that specularly reflected from the black Si are mutually incoherent with respect to each other. As such, the PSF from specular reflection off the Al and the PSF from specular reflection off the black Si do not interfere, but rather add by intensities. The two PSFs are shown in the left-hand panel of Fig. 14. The brightness of the black Si PSF in the dark hole region is shown in the right-hand panel of Fig. 13, for R_s=1, normalized by the Al PSF peak I_0. For any real value of R_s, the contribution of the black Si PSF to the dark hole is the curve on the right-hand panel of Fig. 13, multiplied by R_s.

The performance of the SPC is most closely tied to the contrast performance near the coronagraph inner working angle, which is ~4 λ/D for this design. From the right-hand panel of Fig. 13, the black Si contribution in the neighborhood of 4 λ/D is approximately 3×10^{-3}. Thus, to keep the black Si contribution to acceptable levels, e.g. < 3×10^{-10} at 4 λ/D, a specification of $R_s < 10^{-7}$ is needed.

The diffuse reflectance of the black Si creates a near-uniform illumination of the dark hole region, mutually incoherent with respect to the PSF reflected off the Al. The scattering angles at the shaped pupil that correspond to the dark hole region at the science camera are measured in units of (λ/D_{SP}), which for λ = 550 nm, D_{SP} = 22 mm,

$$\lambda/D_{SP} = 2.5\times10^{-5} \text{ rad}$$

The Lambertian distribution is $I \propto \cos(\theta)$, meaning that it varies on angular scales of radians. The diffuse reflected light can be considered to be constant at $I/I_{in} = R_d/\pi$ ster^{-1} out to >> 1000 λ/D, where R_d is the diffuse reflectance, $0 < R_d < 1$. From dimensional arguments alone, it could be expected that $I/I_0 \sim (\lambda/D_{SP})^2 \sim 10^{-9}R_d$. Calculating the fraction of the illuminated pupil occupied by black Si (as opposed to Al), and normalizing to the peak Al PSF intensity, the proper comparison of intensities produces

$$I/I_0 = 1.3\ R_d\times10^{-9}$$

Thus, a specification of R_d < 1% limits the diffuse reflectance contribution to the contrast in the dark hole to 1.3×10^{-11}.

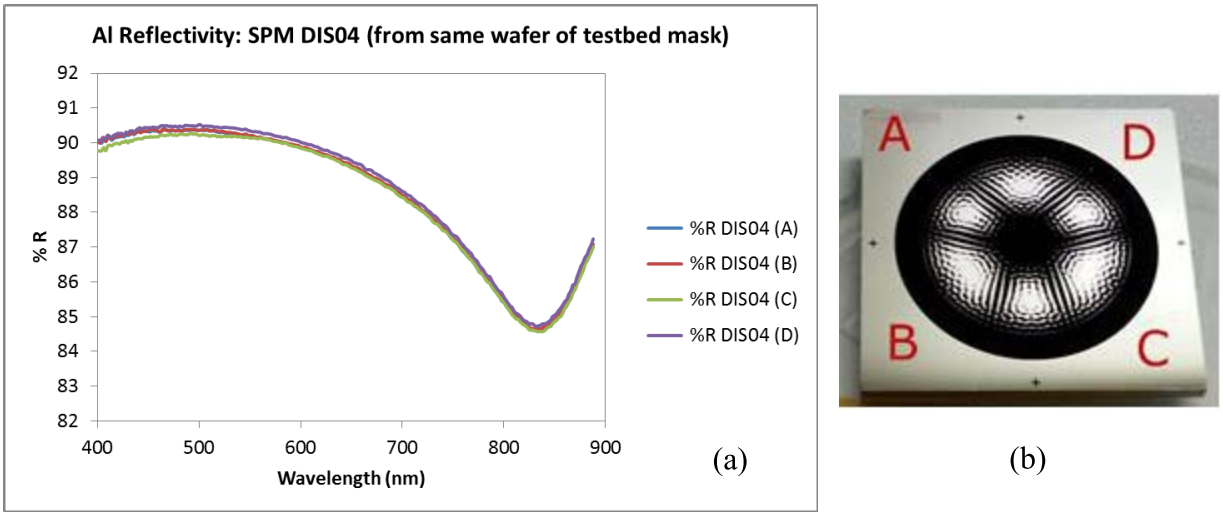

Figure 14 (a) Reflectance of Al regions on the fabricated mask, measured at 8° AOI with PE1050 spectrophotometer; (b) 4 locations (A, B, C and D) on the mask where the Al reflectance was measured. The characteristic reflectance dip of Al at ~850nm is seen above.

5.2 Reflectivity and uniformity of reflective regions after fabrication

The shaped pupil masks being relatively large (>20mm dia on a 35mmx35mm substrate) compared to focal plane masks, and considering the many chemical and low temperature process steps in fabricating these masks, one of the main concerns was about the reflectance of the aluminum coated regions and its uniformity. We measured the reflectance of the mirror regions on the fabricated masks over the full spectrum of interest with a Perkin Elmer 1050

spectrophotometer. Figure 14 shows the reflectance at four different corners of one of the masks with less than 0.2% variation across the mask, which results in no significant impact in contrast performance. Reflectivity variation less than 1% across the mask is fully correctable with a DM stroke of ~ 4nm which is within 1% of the total DM stroke.

The impact of aluminum reflectance variations on contrast can be analyzed based on a previously derived analytic model[30] (Shaklan & Green, 2006). Referring to the Shaklan & Green model, we consider an optic having a weak periodic surface deformation of N cycles across a beam of diameter D, with rms surface height s, reflectance (amplitude) rms $A << 1$ and phase amplitude $\alpha << 1$ radians. Collimated light reflects from the surface, propagates a distance z to the pupil (or pupil conjugate) plane with a wavefront corrector (deformable mirror) DM_p, and then reaches to second deformable mirror DM_{np}. The optical surface reflectance variation (amplitude modulation) would then cause two main effects:

Zero-order (amplitude) effect, which is fully correctable with DM amplitude control using DM stroke given as:

$$s_{DM} = D^2 r / 8\pi^2 z_{DM} N^2$$

where D is the beam diameter; r is the reflectance non uniformity; z_{DM} is the distance between two DMs, and N is the spatial frequency in cycles/aperture.

First-order (amplitude-to-phase cross coupling) propagation effect, which is not fully correctable over bandwidth with DM phase control; the residual contrast is proportional to the propagation distance to DM:

$$C = \frac{1}{6R^2} \cdot \left(\frac{\pi r z \lambda_o N^2}{2D^2} \right)^2$$

where R is the spectral resolution, and z is the propagation distance to (pupil) DM.

For the shaped pupil mask located at a pupil plane, there is no first order effect, while the zero order amplitude effect can be fully corrected using just a fraction of the available DM stroke. In our case, the measured reflectance nonuniformity is $r \approx 1\%$, $N = 4$, $D = 22$mm, $Z_{DM} = 1$m. Thus, the DM stroke needed to fully correct RSP mask Al coating reflectance nonuniformity is $s_{DM} \approx 4$ nm peak-to-valley, which is <1% of DM stroke available in the baselined AOX Xinetics DMs.

5.3 Silicon wafers for the masks with acceptable wavefront quality

Typically thin silicon wafers available off the shelf from the semiconductor industry have acceptable surface roughness better than 5Å rms. However, they are optically very poor. Their surface flatness quality and consequent reflected wavefront with very large curvature and astigmatism make them unsuitable for a coronagraph mask. Wavefront error (WFE) of the RSP mask in its testbed mount was measured using a Zygo interferometer. The rms wavefront error measured was ~20nm after removing the large curvature/focus error in the early version of the chosen wafer used for Milestone 1 and 2 masks.

In principle, the low order RSP mask surface errors are fully correctable with a pupil plane DM. However, due to discreteness of DM actuators, this correction may not be smooth if large DM strokes are needed for significant correction. This will result in residual wavefront error that requires further EFC (Electric Field Conjugation) wavefront control. The impact on contrast due to SP mask surface error (or its DM corrected residual wavefront error) was modeled using PROPER diffraction model (Krist *et al*[31,32], 2014, 2015) with EFC control.

First, post EFC control contrast for the designed SP mask was obtained. Then low order Zernike wavefront error terms of interest (Z4 – Z8) were added to the SP mask design, one at a time, ranging from 0.01 to 0.3 λ rms. Before applying EFC control, the pupil plane DM1 was fitted to the WFE to get its initial setting, simulating the correction of low order mask WFE. We then evaluated post-EFC control contrast for each case. The simulation results are shown in Fig. 15. In general, the contrast change due to individual Zernike term WFE is less than 10^{-10} if the term is smaller than 0.05 λ rms.

For the SP mask installed in the testbed, WFE of 19.6 nm rms was measured, or 0.036 λ rms after removing the focus term (which is accommodated during alignment by translating the field stop and camera). The upper bound on the post EFC contrast deterioration due to RSP mask wavefront error is 7×10^{-11}.

Highly polished 2 to 5 mm thick wafers with better than λ/10 rms surface quality over a 100 mm dia were specially ordered and procured subsequently for fabricating the next generation of SPC masks. Measured wavefront from one of the recently procured 4 mm thick wafers shows significantly better surface quality (~0.03wv rms over the 100mm dia wafer) as seen in Fig. 16.

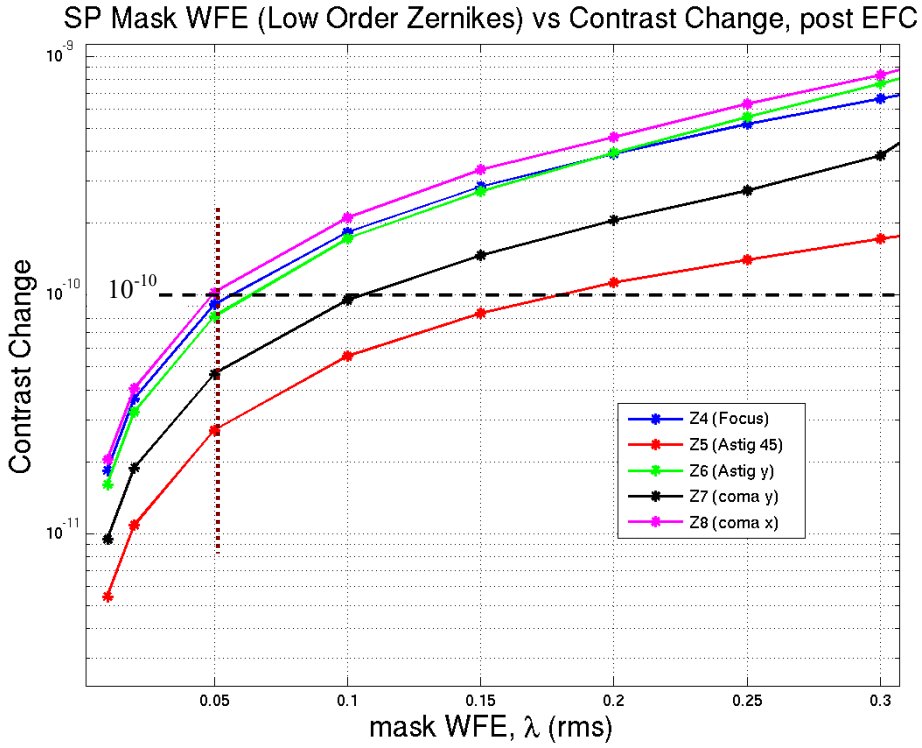

Figure 15. Contrast change vs low order Zernike term mask WFE

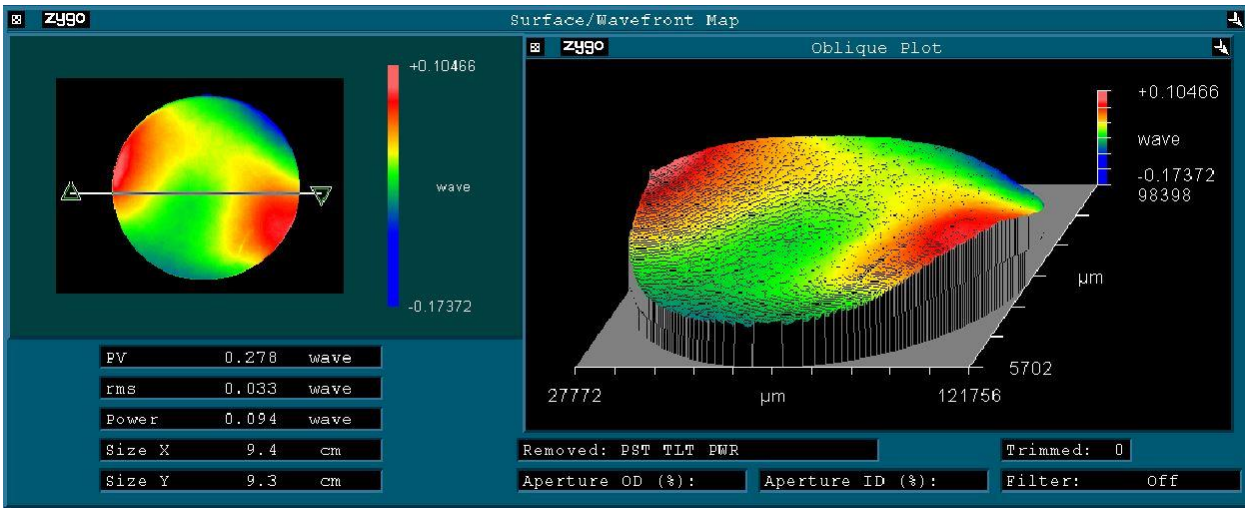

Figure 16. Wafer surface map derived from reflected wavfront map from a 4mm thick silicon wafer as measured by a Zygo interferometer. This wafer is employed for Gen2 SPLC mask currently installed in the HCIT for broadband tests: Surface error = 0.033 wv rms at 633nm over 94% of the full 100mm dia wafer.

5.4 Fabrication with required feature accuracies

Our first set of SPC masks for the AFTA coronagraph testbed were designed with 22 micron minimum feature size based on the full beam dia of 22mm in the HCIT as configured for SPC. The Princeton University team designed the two kinds of reflective SPC masks: 1) the "Disk Science mask" (which has a 360 degree dark hole region but with poorer inner working angle) and 2) the "Characterization mask", (which provides an azimuthally limited dark hole area but a deeper contrast and better inner working angle) to enable spectroscopic characterization of potential planets that may appear in the discovery region. These pupil masks and associated focal plane masks were fabricated by the processes described earlier in Sec. 3 and Table 1. Fabricated masks were imaged with high resolution scanning optical microscope and characterized to estimate fabrication errors and defects. Full images, consisting of >225 sub images stitched together, were assembled to enable detailed performance modeling of the fabricated mask. Images of two such masks fabricated and tested are shown in Figs. 17 (a) and (b) with zoomed-in views in Figs. 18 (a) and (b).

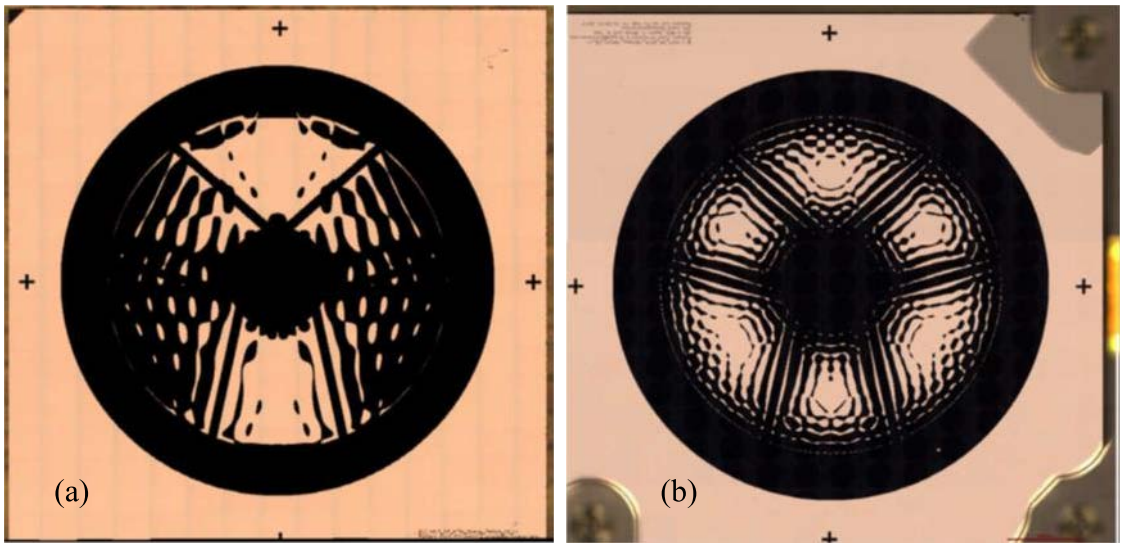

Figure 17. (a) Microscope image of a Characterization mask. Faint grid structure is due to image stitching artifacts of >225 sub-images. Colored tint is due to microscope illumination. (b) Microscope image of a Disc Science mask. High resolution images have been examined and used for modeling the impact of defects on performance

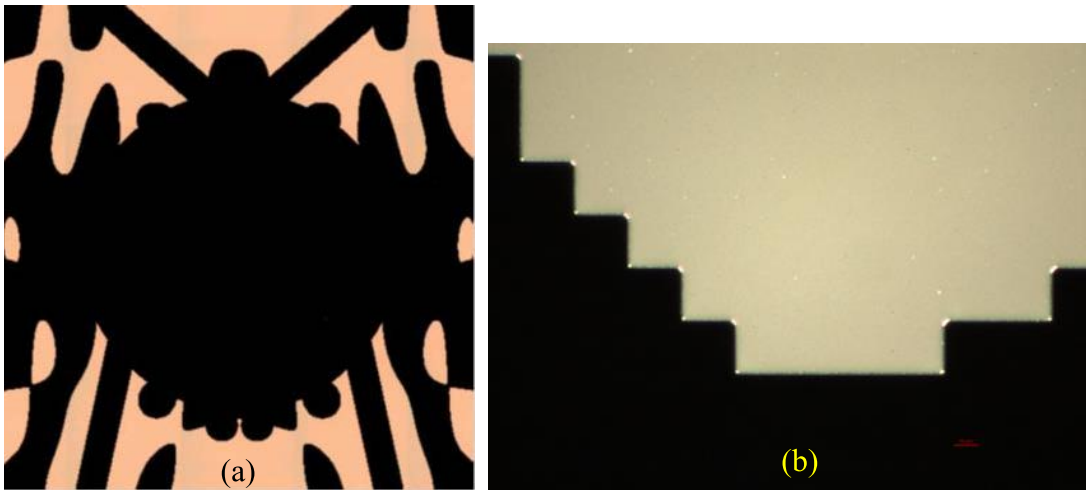

Figure 18. (a) Features in the central region of the characterization mask shown in Fig. 17(a). (b) High resolution image showing 22 μm minimum features. The minor round off errors at the feature corners caused no performance impact in the HCIT experiment.

Edge definition, feature accuracy and defects were analyzed with high resolution images. While initial masks showed about +/-1 micron edge shrinkage (Fig. 19 (a) due to the line width contraction in the contact lithography employed, process improvements have subsequently yielded masks with better than +/-0.5 micron accuracy as shown in Fig. 19 (b). Ultimately, bypassing the contact lithography step and employing direct e-beam writing on the wafer that we plan to adopt for flight hardware would yield significantly better line width accuracy. Defects in the form of minor scratches, pin holes and inclusions were identified over the mask and modeled. The defects identified on the mask that was installed in the testbed for Milestone 2 are shown in Fig. 20.

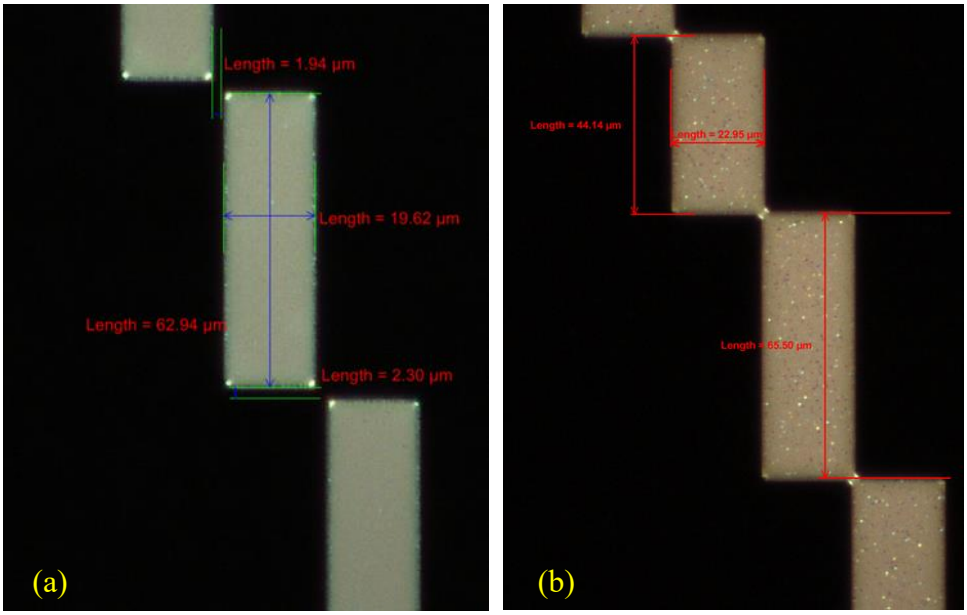

Figure 19. (a) High resolution image of minimum features on the mask at the first iteration showing about 1 micron over etch of edges causing a ~ 2 micron gap at the connecting corners; (b) High resolution image of minimum features on the mask after process improvements showing near perfect edges with no gap at the connecting corners.

5.5 Impact of small defects

Since the RSP mask is at a pupil plane, it is expected to be rather tolerant of manufacturing defects such as minor scratches in black silicon and aluminum after DM wavefront control is applied. This was confirmed by simulations performed using SPC PROPER model (Krist, *et al*[31,32], 2014, 2015) for the installed mask with as-measured defects.

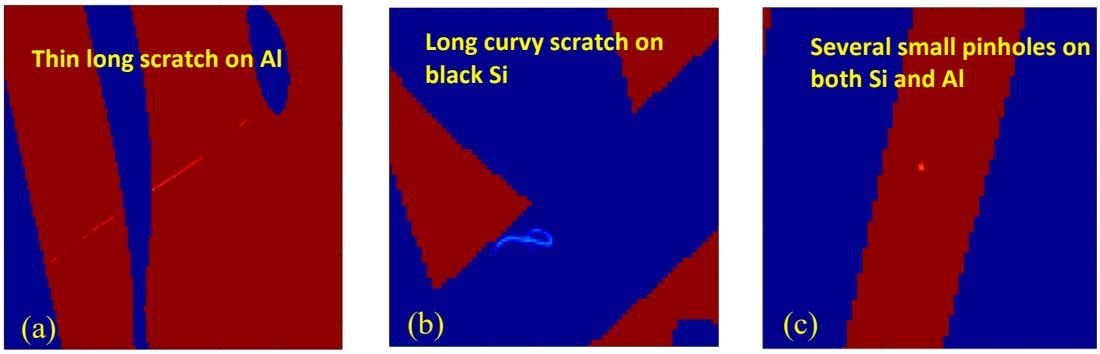

Figure 20. Isolated defects in manufactured mask installed in the test bed. (a) A 0.5mm long scratch on Al (b) a curvy scratch on black silicon region (c) a pin hole. The mean contrast change due to these isolated mask defects after wavefront control was estimated through models to be ~ 7.7×10^{-12}.

The defects identified from high resolution images of the fabricated Milestone 2 mask are about half dozen small spots of 10~30 μm in size on either black Si or Al. Additionally, there is one thin scratch of about 0.5mm in length on Al, and another ~100μm length curvy scratch on black Si (Fig. 21). To model the impact of these defects on SPC contrast, the original design mask of 1000x1000 pixel size (22mm diameter physical size) was block up-sampled to 2000x2000 pixel size for a resolution about ~10μm/pixel (even larger resolution would be preferable, but is currently limited by EFC calculation speed). Post-EFC wavefront control contrast was then calculated. Defects observed in the high resolution scanned manufactured mask were then implanted into the model and post-EFC contrast was recalculated. The mean contrast change due to isolated mask defects after wavefront control is 7.7×10^{-12}. This mask performed in the testbed as expected with demonstrated monochromatic contrast of ~6×10^{-9} averaged across the dark hole (see Riggs *et al*[26], 2014, Zimmerman *et al*[27] 2015, and Cady *et al*[12], 2015 for further details). Subsequent mask designs (Gen2 SPLC) for testbed configurations employing 14 mm beam diameter and a Lyot Stop require 14 micron minimum feature size and these have also been fabricated successfully with current baseline techniques.

6. FOCAL PLANE MASKS MATCHING THE SHAPED PUPIL MASKS

Focal plane masks to selectively transmit light in the dark hole regions in the final image reaching the science camera are fabricated on SOI wafers with a process similar to the one adopted for transmissive shaped pupil masks described in Sec.1. Examples of a "semi-circular" and a "bow-tie" shaped focal plane mask with transmitting apertures between the inner and outer working angles of the dark hole are shown in Fig. 21.

In order to reduce the scattering, polarization, surface plasmon and waveguiding effects[33,34,18] due to the finite thickness and rough walls of the slit edge, we subsequently developed a technique to incorporate a thin membrane on the light incident side which ultimately defines the transmitting slit edges of the mask. A low-stress membrane quality silicon nitride is grown via Low Pressure Chemical Vapor Deposition (LPCVD) on the SOI wafer and then the various etching steps are carried out per Table 1 on both sides of the wafer, which results in a thinner slit edge defined by the 1 or 2 micron thick nitride membrane as shown in the SEM image of the cross section of such a sample in Fig. 22.

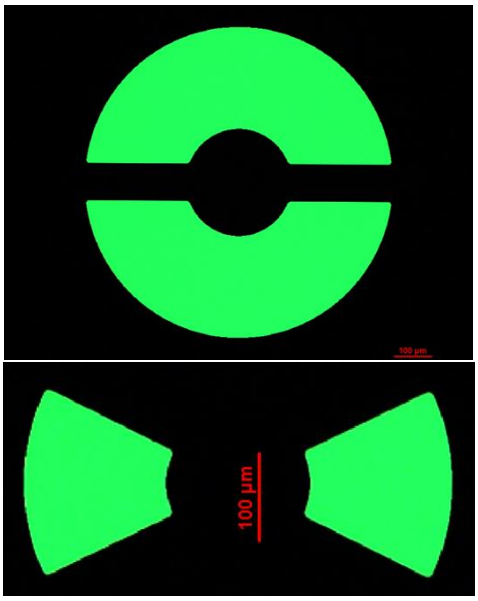

Figure 21. Microscope images of fabricated focal plane masks to transmit light through chosen dark hole regions in the image on the HCIT SPC testbed. The above transmission images were taken with filtered green light.

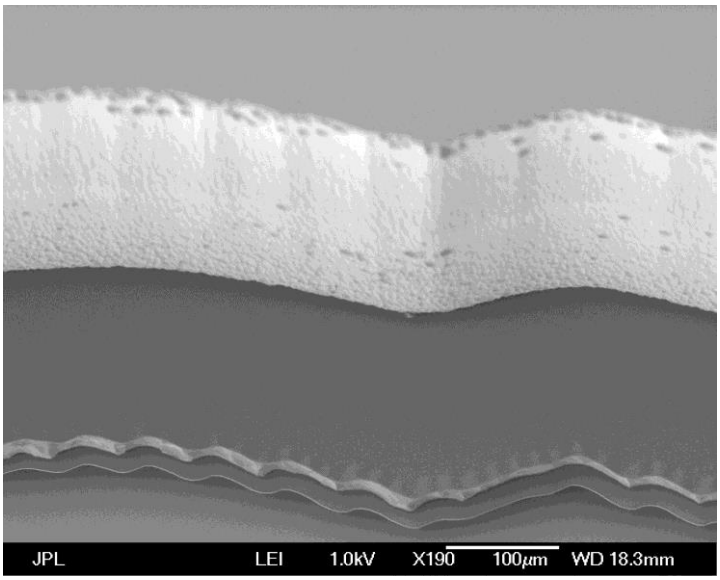

Figure 22. SEM view of an edge showing the 1 micron thin SiN membrane that defines the mask shape and edges. This particular example image is of a small scale star shade mask edge discussed in section 11. The recessed 30μm thick device layer of the wafer and 200 μm recessed step of the full thickness wafer are clearly seen here. Such a cross section reduces sidewall scattering and waveguide effects.

7. LABORATORY DEMONSTRATION

To meet WFIRST-AFTA technology development Milestone 2, a set of SPC masks which passed the Milestone 1 criteria on fabrication was chosen along with corresponding focal plane "bow-tie" masks and installed in the HCIT. Details of the experiments can be found in a companion paper (Cady, *et al*[12] 2015). Three independent sets of data were collected and the estimated mean contrast level from run to run was significantly below the milestone threshold contrast of $1x10^{-8}$ in the dark hole region from 4.4 – 11.2 λ/D defined by the bow-tie focal plane mask geometry.

8. SUMMARY OF PERFORMANCE IMPACT DUE TO DEFECTS AND IMPERFECTIONS

Table 2. Estimate of contrast performance impact due to mask defects, imperfections and aberrations

Mask Imperfection Type	Measured Level	Impact on contrast after WF control	Comments
Black silicon reflectivity, specular	$<7*10^{-8}$	$<2.1*10^{-10}$	Upper bound only (no detection); limited by measurement setup
Black silicon reflectivity, diffuse	<0.6%	$<10^{-11}$	
Mask WFE	~0.036λ rms (above focus)	$7*10^{-11}$	- Post WF control - Better wafers received for future masks
Isolated defects	Several small pinholes and 2 scratches	$8*10^{-12}$	Post WF control
Aluminum reflectivity variations	~0.5%	fully correctable	Post WF control, not including chromatic effects
Total		**$<3*10^{-10}$**	**Upper bound**

9. FURTHER DEVELOPMENTS ON SPC MASKS

The recent innovation of incorporating a Lyot stop in the shaped pupil coronagraph architecture (Fig. 23) has enabled designs with smaller inner working angle at a given contrast and throughput, significantly improving the compatibility of SPC solutions with obscured apertures (Riggs[27] *et al.,* 2014; Zimmerman *et al*[28]., 2015; Carlotti *et al*[35]., 2015).

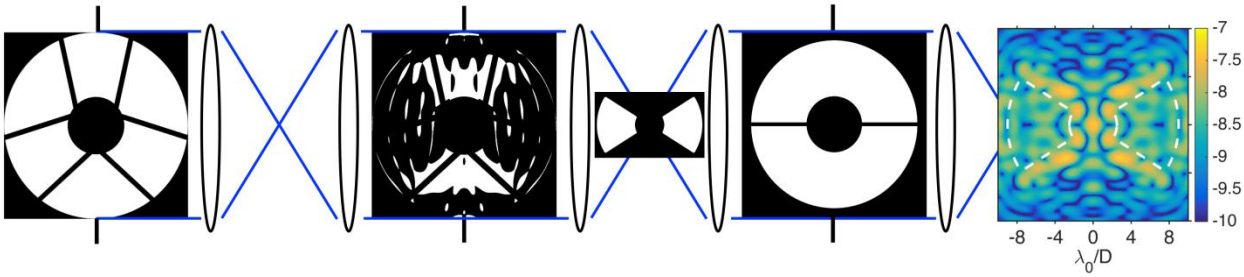

Figure 23. Propagation schematic for the new Lyot configuration of the shaped pupil coronagraph (SPLC). This is a characterization mode SPC designed to produce a dark hole with inner working angle 2.8 λ/D, with a bowtie-shaped field of view over a broad band up to 10 and 18% bandwidths. The first focal plane after the shaped pupil is occulted by a hard-edged bowtie mask. In the following pupil plane, a Lyot stop serves to further reject on-axis starlight. In the final focal plane, the residual starlight is constrained to a contrast factor 10^{-8} or below the peak of the star.

The characterization mode design of SPLC mask, shown in the right hand side of Fig. 12, has an inner working angle of 2.8 diffraction widths, and reaches contrast 10^{-8} or below throughout a bowtie-shaped field of view over an 18% bandwidth. See Zimmerman *et al*[28] paper for a more detailed discussion of the concepts behind the shaped pupil Lyot coronagraph (SPLC), and the methods used to optimize and evaluate the designs.

Such an SPLC characterization mask with the 14 μm minimum feature size per design was fabricated (Fig. 24) and installed in the HCIT static testbed in Feb 2015 to demonstrate the required broadband performance to meet WFIRST-AFTA coronagraph instrument Milestone 5 criteria.

Lyot stops and focal plane masks matching the SPLC static testbed were also designed, fabricated and installed in the testbed along with the SPLC mask. Several bow tie focal plane masks were fabricated on an SOI chip following the basic techniques described in section 1. Figure 25 (a) shows the array of these bow tie focal plane masks on one chip while Fig 25 (b) shows a detailed view of one them.

Similarly, Lyot stops as shown in figure 26 were fabricated on SOI wafers. The microscope image of one of these Lyot stops on a mount (Fig 26 (a)) taken in transmission as well as reflection mode is shown in Fig 26 (b). The central opaque circle is nominally 420 μm in radius supported by 56 μm wide struts along a diameter as shown.

Test details and initial results with these SPLC masks can be found in Cady *et al*[12].

Figure 24. Microscope image of SPLC mask installed in the testbed for Milestone 5 tests

The next generation characterization-mode SPLC mask to be installed on the Occulting Mask Coronagraph (OMC) dynamic testbed at JPL will have slightly modified physical features to match the new testbed layout geometry. This testbed will incorporate a scale model of the telescope, wavefront disturbances, and both low- and high-order wavefront control. On the dynamic testbed, the telescope pupil diameter at the shaped pupil is 19.7 mm, so each binary element in the mask is a 19.7 micron square. The binary pattern will be stretched horizontally to account for an 8 degree incidence angle. A disc science mode SPC design will also makes use of a Lyot configuration.

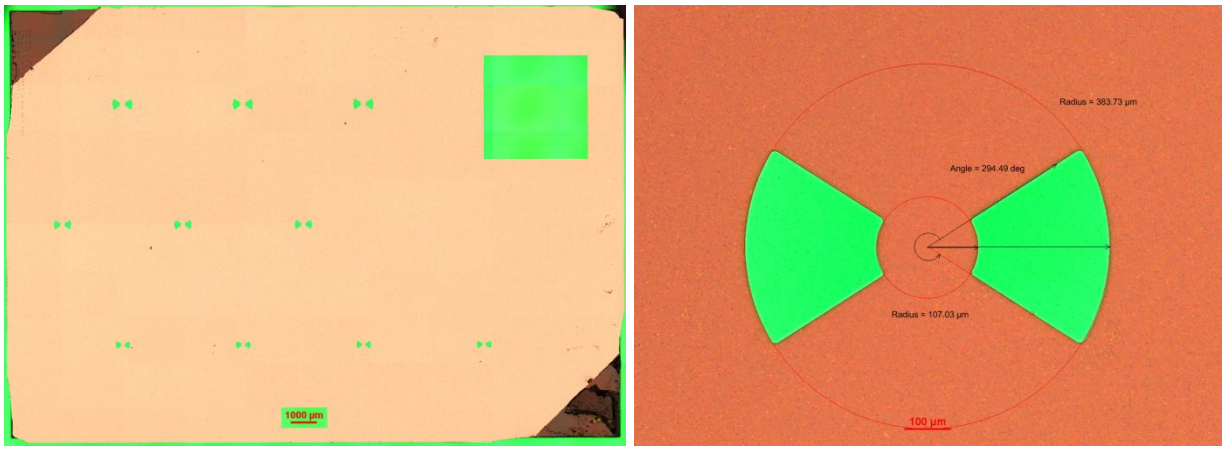

Figure 25. (Left) A high resolution microscope image, in transmission, of the array of SPLC bow tie focal plane masks. These masks were designed for different center wavelengths. (Right) A high resolution microscope image, in transmission, of one of the bow-tie masks.

Figure 26. Lyot Stop for SPLC static testbed. (Left) Lyot Stop on a mount. (Right) High resolution microscope image in combined reflection and transmission mode of the same Lyot Stop.

10. TRANSMISSIVE SPC MASKS

Progress has also been made in the development of techniques to produce transmissive SPC masks with very low ghost reflections and dispersion. We have developed a concept and methodology to fabricate these masks on fused silica glass with nanostructures to provide <0.1% specular reflection over a broad spectral band. Together with a small wedge angle (~0.01 deg), these low dispersion glasses with low reflection can support transmissive SPC masks with island structures. We have recently produced a few such masks on nanostructured glass (Hobbs *et al*[36,37], 2007, 2013) procured from Telaztec LLC, with satisfactory physical characteristics; these preliminary fabrication results encourage and guide further technology development.

11. LABORATORY SCALE STAR SHADE MASKS

An alternative to the internal coronograph is the external occulter, or starshade. A starshade is a flower-shaped screen ~30-40 m in diameter positioned ~30,000 – 40,000 km in front of the telescope directly in the line of site to a target star. The starshade is shaped to control the diffraction of light and form a dark shadow around the telescope. It blocks the starlight but appears to be so small that light from planets orbiting the star passes around the starshade and is directly imaged by the telescope. From the first practical starshade design (Cash[38], 2006) to the latest round of designs, taking into account engineering and launch constraints (Seager[39] *et al*, 2015), starshades have been shown to be an effective means of detecting exoplanets without imposing tight constraints on the telescope and instruments. Because of its large size and separation, full-scale end-to-end optical testing is not possible without launching a starshade and telescope into deep space. Sub-scale optical tests are thus used to validate the optical propagation models. The next round of testing will employ smaller masks and longer optical paths so that the experiments use the same Fresnel number (~12) as the flight geometry. This is important because it validates the optical models using the same diffraction equations that describe the flight system.

Several experiments over the last decade have been done to demonstrate the principle of starshades with few-cm scale masks, including laboratory testing by Schindhelm *et al*[40] (2007), Leviton *et al*[41] (2007), Samuele *et al*[42] (2009), and Cady *et al* [43,44](2009). Additionally, testing of a half-meter starshade in a dry lakebed has also been reported (Glassman *et al*[45], 2013).

The tests were successful in demonstrating high contrast in the transparent regions between petals. Additionally, the residual scattered light seen around the perimeter of the starshade is well explained by models that account for mask manufacturing resolution and tolerances (Sirbu, Ph.D. Dissertation[46], 2014).

11.1 Initial Designs and Fabrication of Small Star Shade Masks for Laboratory Tests

Small size (~ 100 mm diameter) laboratory scale star shade masks were designed by the Princeton University team. These were fabricated at JPL by e-beam lithography and deep reactive ion etching (DRIE) for testing at the Princeton starshade testbed (Cady *et al*[43] 2009, Sirbu *et al*[47-50] 2014, 2011, 2013, 2015). The first generation of these masks were designed and optimized with 2 micron edge feature accuracy for ease of manufacturing. Subsequently, masks with 0.5 micron pixel resolution have been designed and fabricated. SOI wafers with a 50 micron device layer were employed for these initial masks. Figure 27 shows a picture of a flower shaped mask with 16 petals on a 100 mm dia SOI wafer. Etching is done from both sides in two steps to create the transmitting petal shapes with the step cross section as shown in Fig. 2. A high resolution image (Fig. 27 (b)) of one of the petals reveals the structure and edge shape.

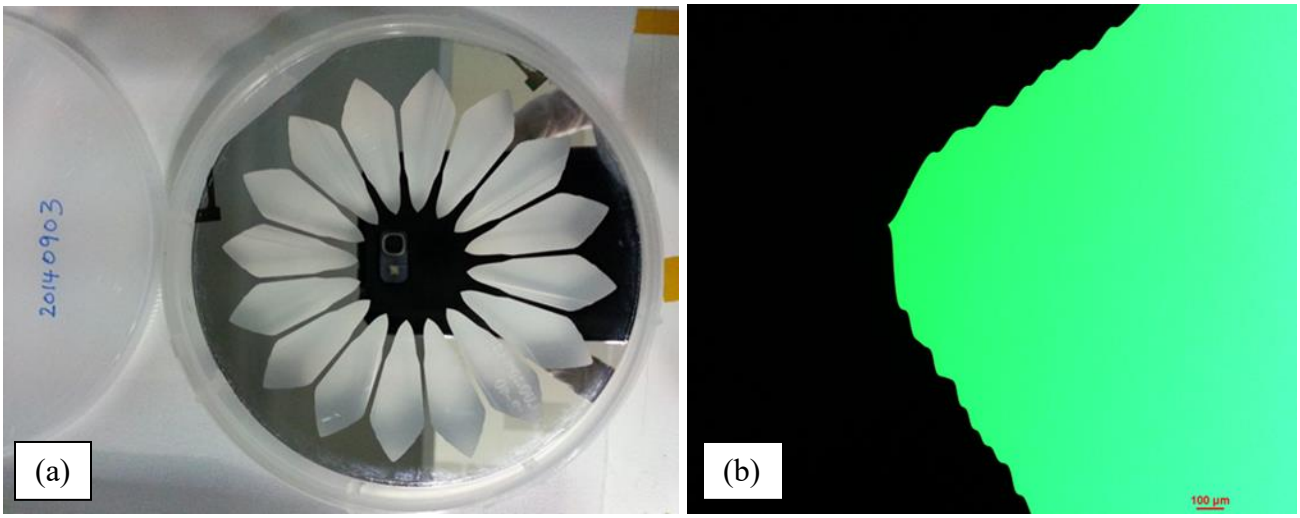

Figure 27. (a) A picture of a lab scale star shade mask on a 100mm dia SOI wafer. (b) High resolution microscope image of one of the petal edges.

For further improvements, we will use the same SOI wafer approach as discussed in sections 1 and 6 above with the addition of a 1 um thick layer of silicon nitride so that there is virtually no wall thickness at the diffracting edge. The SEM image in Fig. 22 shows the thin membrane and edge definition achievable with this approach. Numerical and analytical models of these masks predict that with 0.25 µm resolution accuracy, they will provide pupil suppression and image-plane contrast consistent with flight requirements (Sirbu[46,47] 2014, 2015). The next round of fabrication of such lab scale star shade masks on a 6 inch SOI wafer is now getting ready with the required 0.25 µm resolution design specs.

12. SUMMARY AND CONCLUSIONS

Masks are among the key components of a high contrast coronagraph instrument. Innovative approaches have been developed to design, fabricate and test masks of various kinds. Critical technologies include back silicon technology through cryogenic reactive ion etching to fabricate reflective shaped pupil masks, and e-beam lithography and deep reactive ion etching to fabricate precisely shaped slits with very thin membranes. These masks have been fabricated successfully with laboratory tests demonstrating key milestones for WFIRST –AFTA program, accomplishing <1e-8 contrast in narrow band in the lab, paving the way for similar performance in broad band to be demonstrated in Sep 2015. A summary of the mask performance in the testbed is given in Table 2 reassuring the current level of maturity in fabrication technology for such devices. The reflective shaped pupil mask technology is thus mature for demonstrating TRL 5 readiness in 2016. Similarly, laboratory scale star shade masks have been fabricated successfully with models estimating their performance in the lab and guiding next versions with finer resolution and accuracy.

13. ACKNOWLEDGEMENTS

The research reported here is performed at the Jet Propulsion Laboratory, California Institute of Technology, under a contract with the National Aeronautics and Space Administration.

14. REFERENCES

[1] Trauger, J. T. and W.A. Traub, "A laboratory demonstration of the capability to image an Earth-like extrasolar planet", Nature, Vol.446, pp. 771-773. (2007).

[2] Moody, D. C., B. L. Gordon, J.T. Trauger ,"Design and demonstration of hybrid Lyot coronagraph masks for improved spectral bandwidth and throughput", Proc. of SPIE 7010, 70103P, (2008).

[3] Trauger, J., *et al.*, "Complex apodization Lyot coronagraphy for the direct imaging of exoplanet systems: design, fabrication, and laboratory demonstration", Proc. SPIE. 8442 (2012).

[4] Trauger, J., D. Moody, and B. Gordon, "Complex apodized Lyot coronagraph for exoplanet imaging with partially obscured telescope apertures," Proc. SPIE 8864, 12 (2013).

[5] Belikov, R., *et al*., "Towards 10^{-10} Contrast for Terrestrial Exoplanet Detection: Demonstration of Extreme Wavefront Correction in a Shaped-Pupil Coronagraph", Proc. SPIE 6265-42, (2006)

[6] Carlotti, A., N. J. Kasdin, and R. J. Vanderbei, "Shaped pupil coronagraphy with WFIRST-AFTA," Proc. SPIE 8864, 10 (2013).

[7] Guyon, O. "Exoplanet Imaging with a Phase-induced Amplitude Apodization Coronagraph. I. Principle" . *Astrophysical Journal ApJ 622* , 744. (2005).

[8] Guyon, O., F. Martinache, R. Belikov, R. Soummer, "High performance PIAA coronagraphy with complex amplitude focal plane masks" ,The Astrophysical Journal Supplement, Volume 190, Issue 2, pp. 220-232, (2010).

[9] Guyon, O., P. M. Hinz, E. Cady, R. Belikov, and F. Martinache, "High Performance Lyot and PIAA Coronagraphy for Arbitrarily Shaped Telescope Apertures," ApJ 780, 171 (2014).

[10] Kern, B., *et al*, "Laboratory demonstration of Phase Induced Amplitude Apodization (PIAA) coronagraph with better than 10^{-9} contrast", presented in Optics & Photonics SPIE 2013; also, NASA ROSES TDEM PIAA Milestone 1 Report (2013), and in Journal of Astronomical Telescopes, Instruments and Systems, submitted (2015)

[11] Kern, B., *et al*, "PIAACMC Mask Fabrication, Characterization, and Modeling for WFIRST-AFTA", Journal of Astronomical Telescopes, Instruments and Systems, JATIS, submitted (2015).

[12] Cady, E., *et al,* "Demonstration of high contrast with an obscured aperture with the WFIRST-AFTA shaped pupil coronagraph", Journal of Astronomical Telescopes, Instruments and Systems, submitted (2015). Also, see an article in this issue of the SPIE proceedings 9605 (2015).

[13] Belikov, R., A. Give'on, B. Kern, E. Cady, M. Carr, S. Shaklan, K. Balasubramanian, V. White, P. Echternach, M. Dickie, J. Trauger, A. Kuhnert, and N.J. Kasdin, "Demonstration of high contrast in 10% broadband light with the shaped pupil coronagraph," Proc. SPIE 6693, pp. 66930Y–1 – 66930Y–11 (Sept. 2007).

[14] Pueyo, L., J. Kay, N.J. Kasdin, T. Groff, M. McElwain, A. Give'on, and R. Belikov, "Optimal dark hole generation via two deformable mirrors with stroke minimization," Applied Optics 48(32), 6296–6312 (2009).

[15] Balasubramanian, K. *et al*, High contrast internal and external coronagraph masks produced by various techniques, Proc. SPIE 8864-62 (2013).

[16] Balasubramanian, K., *et al*., "Fabrication and Characteristics of Free Standing Shaped Pupil Masks for TPF Coronagraph," Proc. of SPIE, 6265 (2006).

[17] Riggs, A.J.E, J.N. Kasdin, and T.D. Groff, "Recursive starlight and bias estimation for high-contrast imaging with an extended Kalman filter", Journal of Astronomical Telescopes, Instruments and Systems, submitted (2015)

[18] Groff, Tyler D., "Optimal Electric Field Estimation and Control for Coronagraphy," Ph.D Thesis, Princeton University, (2011)

[19] Groff, T. D. and N. J. Kasdin., "Kalman filtering techniques for focal plane electric field estimation," Journal of the Optical Society of America A 30(1), 128–139 (2013).

[20] Riggs, A.J.E., T. Groff, A. Carlotti, N.J. Kasdin, E. Cady, B. Kern, and A. Kuhnert, "Demonstration of symmetric dark holes using two deformable mirrors at the high-contrast imaging testbed", Proc. SPIE 8864-28, (2013).

[21] Carlotti, A., R. Vanderbei, and N. Kasdin, "Optimal pupil apodizations of arbitrary apertures for high-contrast imaging," Optics Express 19(27), 26796–26809 (2011).

[22] Vanderbei, R., "Fast fourier optimization, sparsity matters," Mathematical Programming Computation, 1–17 (2012).

[23] de Boer, M.J., Gardeniers, J.G., Jansen, H.V., Smulders, E., Gilde, M.J., Roelofs, G., Sasserath, J.N. and Elwenspoek, M., "Guidelines for Etching Silicon MEMS Structures Using Flourine High-Density Plasmas at Cryogenic Temperatures", Journal of Micromechanical Systems, Vol. 11, No. 4, pp. 385-401 (2002).
[24] Dussart, R., Tillocher, T., Lefaucheux, P., Boufnichel, M.., "Plasma cryogenic etching of silicon: from the early days to today's advanced technologies", Phys. D: Appl. Phys., Vol. 47, pp. 1-27 (2014).
[25] Laermer, F., and A. Schilp of Robert Bosch GmbH, "Method of Anisotropically Etching Silicon", US-Patent No. 5501893 (3, 26, 1996).
[26] Laermer, F., Schilp, A., Funk, K., Offenberg, M., "Bosch Deep Silicon Etching: Improving Uniformity and Etch Rate for Advanced MEMS Applications", 12th IEEE International Conference on Micro Electro Mechanical Systems, 17-21 January 1999 (IEEE, Orlando, Fl, USA, 1999), pp. 211-216.
[27] Riggs, A. J. E., N. Zimmerman, A. Carlotti, N. J. Kasdin, and R. Vanderbei, "Shaped pupil design for future space telescopes," Proc. SPIE 9143, 25 (2014).
[28] Zimmerman, N., A. J. Eldorado Riggs, N. J. Kasdin, A. Carlotti, and R. J. Vanderbei, "Shaped Pupil Lyot Coronagraphs: High-Contrast Solutions for Restricted Focal Planes", Journal of Astronomical Telescopes, Instruments and Systems, JATIS, submitted (2015).
[29] Poberezhskiy, I., *et al.,* "Technology development towards WFIRST-AFTA coronagraph," Proc. SPIE 9143 (2014).
[30] Shaklan, S.B, and J. J. Green, "Reflectance and optical surface height requirements in a broadband coronagraph. 1. Contrast floor due to controllable spatial frequencies," Appl. Optics, vol. 45, no. 21, pp 5143-5153 (2006).
[31] Krist, John E., "End-to-end numerical modeling of AFTA coronagraphs", Proc. SPIE, 9143, 91430V (2014).
[32] Krist, J., Nemati, B., Mennesson, B., "Numerical modelling of the proposed WFIRST-AFTA coronagraphs and their predicted optical performances", Journal of Astronomical Telescopes, Instruments and Systems, JATIS, submitted (2015)
[33] Ceperley, D., A. Neureuther, M. Lieber, and J.Kasdin, "Characterizing Edge Generated Stray Light Sources for TPF Coronagraph Pupil Masks" Proc. SPIE 5905, (2005).
[34] Ceperley, D., A. Neureuther, M. Miller, M. Lieber, and J.Kasdin, "Stray-Light Sources from Pupil Mask Edges and Mitigation Techniques for the TPF Coronagraph" Proc. SPIE 6271, (2006).
[35] Carlotti, A., *et al*, "Comprehensive review of shaped pupil coronagraphy: design trade-offs & sensitivity to low-order aberrations." Submitted to Astronomy & Astrophysics (2015).
[36] Hobbs, S.D, B. D. MacLeod, and J. R. Riccobono, "Update on the Development of High Performance Anti-Reflecting Surface Relief Micro-Structures", Proc. SPIE 6545 (2007).
[37] Hobbs, S.D, B. D. MacLeod, and J. R. Riccobono, "Contamination resistant antireflection nano-textures in fused silica for laser optics", Proc. SPIE 8885 (2013).
[38] Cash, W., "Detection of earth-like planets around nearby stars using a petal shaped occulter", Nature, 442, 5153 (2006).
[39] Seager, S., *et al*, Exo-S: starshade probe-class exoplanet direct imaging mission concept final report: http://exep/stdt/Exo-Starshade_Probe_Class_Final_Report_150312_URS250118.pdf (2015)
[40] Schindhelm, E., Laboratory studies of petal-shaped occulters," Proc. SPIE 6693, 669305 (2007).
[41] Leviton, D. B., *et al,* "White-light demonstration of one hundred parts per billion irradiance suppression in air by new starshade occulters," Proc. SPIE 6687, 66871B (2007).
[42] Samuele, R., "Progress at the starshade testbed at Northrop Grumman Aerospace Systems: comparisons with coputer simulations," Proc. SPIE 7731, 773151 (2010).
[43] Cady, E., *et al*., "Progress on the occulter experiment at Princeton", Proc SPIE vol. 7440, (2009).
[44] Cady, E., *et al*, "Broadband suppression and occulter position sensing in the Princeton occulter testbed," Proc. SPIE 7731, 77312F (2010).
[45] Glassman, T., *et al*, "Measurements of high-contrast starshade performance," Proc. SPIE 9143, 91432O (2014).
[46] Sirbu, D., Ph. D. Dissertation, Princeton University, *Occulter-based high-contrast exoplanet imaging: design, scaling, and performance verification* (2014)
[47] Sirbu, D., S. B. Shaklan, N. J. Kasdin, and R. J. Vanderbei, "Scaling relation for occulter manufacturing errors", Proc. SPIE 9605-86, (2015)
[48] Sirbu, D. *et al*, "Optical verification of occulter-based high contrast imaging," Proc. SPIE 8151, 815114 (2011).
[49] Sirbu, D., N. J. Kasdin, and R.J. Vanderbei, "Progress on optical verification for occulter-based high contrast imaging," Proc. SPIE 8864, 886419 (2013).
[50] Sirbu, D., N. J. Kasdin, and R.J. Vanderbei, "Diffractive analysis of limits of an occulter experiment," Proc. SPIE 9143, 91432P (2014).